

# XMM-Newton CCF Release Note

XMM-CCF-REL-396

## EPIC MOS response

Simon Rosen, Richard Saxton, Michael Smith

31 Mar 2023

### 1 CCF components

Name of CCF	VALDATE	EVALDATE	Blocks changed	XSCS flag
EMOSn.REDIST_0121.CCF	2013-04-27	2014-12-16	CCD.REDISTRIBUTION-k	NO
EMOSn.REDIST_0122.CCF	2014-12-16	2016-08-05	CCD.REDISTRIBUTION-k	NO
EMOSn.REDIST_0123.CCF	2016-08-05	2018-03-26	CCD.REDISTRIBUTION-k	NO
EMOSn.REDIST_0124.CCF	2018-03-26	2019-11-14	CCD.REDISTRIBUTION-k	NO
EMOSn.REDIST_0125.CCF	2019-11-14	NONE	CCD.REDISTRIBUTION-k	NO

Where the  $n$  refers to the MOS-1 and MOS-2 cameras in *EMOSn* and,  $k$ , to the 7 CCDs of each camera in *CCD-REDISTRIBUTION-k*.

### 2 Changes

This update reflects a substantial extension of the time base for the MOS redistribution matrices since the last significant update (Sembay et al 2011). We provide redistribution profiles as a function of input photon energy for 5 new epochs, starting from revolution 2450 (April 2013), each generally spanning blocks of 300 revolutions, except the last file, epoch 19, whose application in scientific analysis will cover from revolution 3650 to the current time.

Following the update of the MOS contamination characterisation (XMM-CCF-REL-390), a new set of redistribution matrices are provided, as previously, for both MOS instruments, for patterns 0 (singles) and  $< 12$  (all), and for the patch core, patch wings and off-patch positions, to track the evolution over the period since 2011.

Analysis of the redistribution functions is built upon the updated contamination information. The process uses observed MOS spectra of 3 calibration targets with well characterised, stable X-ray spectra, i.e. 1E 0102-72.3, Zeta Puppis and the soft isolated neutron star, RX J1856.5-3754. To maximise consistency with earlier analyses of the MOS redistribution, we have adopted the spectral models derived from the IACHEC project, as

used in Sembay et al (2011). The empirical redistribution profiles, as illustrated in Sembay et al (2011) (their figure 2), are adjusted via an iterative fitting scheme to optimise the match of the observed spectra to the relevant models. The empirical profile used to describe the MOS response for a given input photon energy,  $e_0$ , is composed of (i) a Voigt function centred at  $e_0$ , with different damping values on its high and low energy wings, (ii) a secondary peak at lower energies, whose peak energy varies with  $e_0$  and position on the detector, its low energy wing being a Voigt profile and its high energy wing being a linear decay, and (iii) a flat shelf function, subject to a Voigt-damped high-energy tail and a half Gaussian function at its low-energy end; the shelf is flat between 100 eV and  $e_0$ . The model comprises 16 fitted parameters and they are derived for each of a set of input photon energies, yielding an energy-dependent profile for each input photon energy.

Spectra of the calibration sources, when observed off-patch, were extracted in circular apertures of radius 80 CCD pixels (note that although 1E 0102-72.3 is slightly extended, it is treated as point-like when correcting for the PSF). For observations on patch, spectra were extracted from a circular region of radius 14 CCD pixels (15.4 arcsecs: MOS pixels cover 1.1 arcsecs on the sky), centred on the core position and patch wing measurements were taken from a co-centred annular region between 14 and 36 CCD pixels. The extraction of spectra was performed using the XMM-Newton SAS 20 release.

For 1E 0102-72.3, the IACHEC model represents an average over the remnant and in that context, the analysis takes no account of spatial variations of the spectral profile across the remnant image: it is acknowledged that while the source shows broadly consistent spectral profiles when extracted from different radial annuli centred on the source, there are relative differences in the strengths of the oxygen and neon lines of up to 25% between spectra extracted from the eastern and western halves of the remnant. Such variations can introduce uncertainties into the response analysis. We note that in the 'on patch' observations of 1E 0102-72.3 the source is well centred on the patch, with the prominent emission ring of the remnant being broadly concentric with, and of similar radius to, the circle defining the patch core. We also note that in the cases of RX J1856.5-3754 and Zeta Puppis, while the analysis assumes that the source is centred in the extraction region, in some 'on patch' observations, the source centre is displaced from the patch centred by as much as 17 arcsecs. Although the impact on the encircled energy fraction (EEF) of the PSF can then be substantial (because the extraction region is centred on the wings of the source PSF, not its centre, and the source centroid position is not taken into account), this is largely absorbed into the spectral normalisation during the fitting process when computing the response functions. Nevertheless, this does not allow for energy-dependent differences in the true and assumed EEFs. Thus, source spectra used for computing the responses in the patch core or wings, but where the source centroid is displaced from the patch centre, will suffer from some energy dependent inaccuracies in their PSF corrections. Using the ELLBETA model PSF, we determined the ratio of the EEF for a centred extraction region of radius 15 arcsecs to that of one offset by 15 arcsecs on the PSF wings; the ratios were computed for both the 0.2 keV and 2.0 keV PSF maps. The difference of the ratio is about 1%, growing to 3.5% if the offset is 23 arcsecs. Thus, although there can be a large absolute difference in the PSF EEF correction factor, there appears to be only a small impact in terms of introducing an energy dependence. We point out that since all the observations of 1E 0102-72.3, and some of the observations

of RX J1856.5-3754 and Zeta Puppis, are generally well centred within the patch core, the energy-dependent impact of using incorrect EEFs for the displaced pointings will be diluted.

In each observation, spectra from each column within the extraction region, for each camera, were screened to exclude columns which showed any evidence of a notable energy offset ( $>20$  eV) relative to the mean of the columns; columns excluded in the previous analyses were generally also excluded. The epochs defined are shown in table 1 while the observations used are presented in table 2. Note that in previous analyses, a potential gain shift was also fitted for each spectrum but this was not included here due to instabilities encountered in the fitting process. The effect of any residual gain shifts should be very small as typically only one spectrum amongst the group of spectra used for a given epoch show evidence of a significant shift (generally even these are  $\leq 5$  eV), so the effect will be diluted by the majority of negligibly shifted spectra.

Table 1: <sup>a</sup> From the beginning of the first revolution to the end of the last in each epoch.

Epoch	Revolution range	Dates <sup>a</sup>
15	2451-2750	2013-04-27 to 2014-12-16
16	2751-3050	2014-12-16 to 2016-08-05
17	3051-3350	2016-08-05 to 2018-03-26
18	3351-3650	2018-03-26 to 2019-11-14
19	3651-3950	2019-11-14 to current date

Figure 1 presents the redistribution functions for 0.3 keV input photons for pattern 0 (single events) for the patch core, patch wings and off-patch locations. Figure 2 shows the profiles for 2 keV input photons.

In both MOS1 and MOS2, for low energy events, the previous, broadly systematic trend continues, with the drift to lower energies of the peak of the low-energy shoulder component, accompanied by the broadening of its low energy wing, especially for the core and wings regions. The trend increases the number of events that are recorded with energies below 0.15 keV. For 0.3 keV events, in the core, around 51% (MOS1) to 61% (MOS2) of events were redistributed to energies in the 0.15-0.5 keV range in epoch 12 while for the new epochs, this is typically reduced to  $\sim 42$  to 50%, respectively.

### 3 Scientific Impact of this Update

As an initial test to gauge the impact of the new redistribution matrices, we performed fits to the spectra of RX J1856.5-3754, from revolutions 3255 (0727761201), and 4000 (0810841901), which were not used in the analysis, and revolution 3903, which was used.

In figure 3 the data and the spectral model, using the old (top) and new (bottom) redistribution matrices, for MOS1 (left) and MOS2 (right) from rev 3255, where the target was on-patch, are presented. The spectral model is the IACHEC two component model

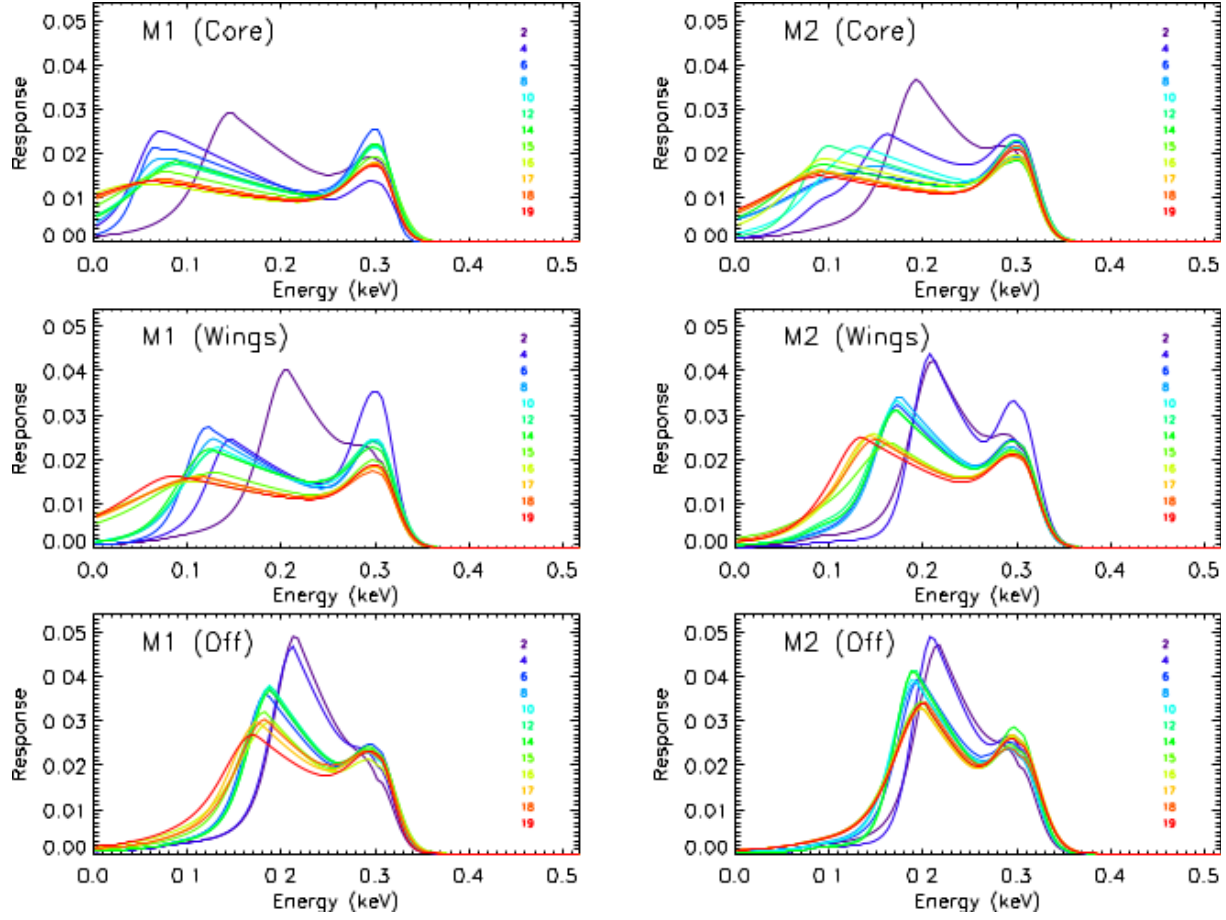


Figure 1: MOS1 (left) and MOS2 (right) redistribution functions for 0.3 keV input photons, for pattern 0. Top: patch core, centre: patch wings, bottom: off-patch. In each panel we show the profiles of existing redistribution CCFs (alternate epochs), from epoch 2 up to epoch 14, together with the profiles of the new epochs, 15-19, delineated in different colours, as indicated in the panels.

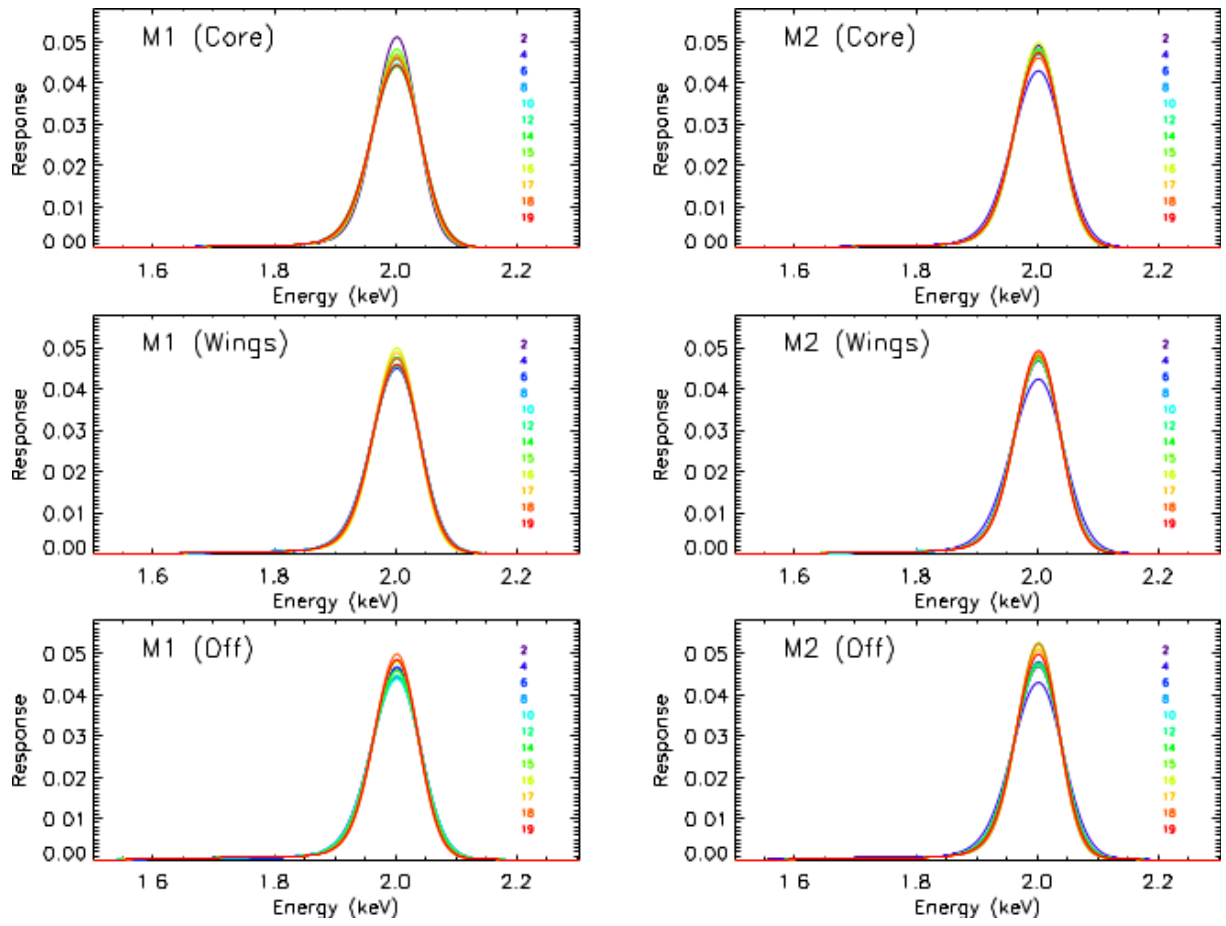


Figure 2: As for figure 1 but for 2.0 keV input photons.

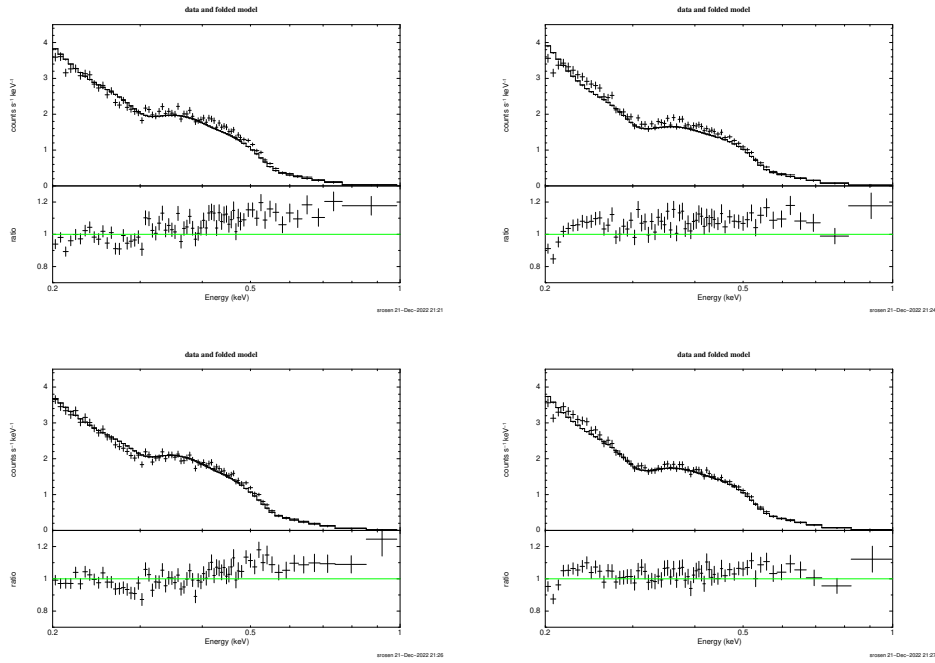


Figure 3: Fits to the spectra of RX J1856.5-3754 obtained in revolution 3255 for MOS1 (left) and MOS2 (right). In the top row, the model events are redistributed using the old redistribution CCFs while the bottom row uses the new ones.

for RX J1856.5-3754 involving two blackbody components with temperatures of 62.8 eV and 32.3 eV, subject to a single cold galactic absorption column of  $1.1 \times 10^{20} \text{ cm}^{-2}$ . The spectral parameters were fixed, except for a global normalisation, which takes account, of, for example, imperfections in the PSF corrections.

In table 3, we present the  $\chi^2$  values using the old and new redistribution functions, for RX J1856.5-3754, from revolutions 3255, 3903 and 4000. In each case, the model was fitted (only a global normalisation factor) to data in the range 0.15-1.0 keV; the  $\chi^2$  values quoted in the table are for the same range.

As can be seen from the table, in all cases for RX J1856.5-3754, fits using the new redistribution functions yield significantly improved  $\chi^2$  values.

We also tested the case of the supernova remnant, N132D. This is an important test source since its spectrum is unlike that of the calibration sources so it should be representative of any other source. Four observations from revolutions 2593 (0414180601), 3149 (0414180901), 3520 (0811012401) and 3701 (0811012401), all observed in MOS large Window mode, were analysed. The source is notably extended and in this case, no correction was made for the PSF, i.e. the PSF correction was assumed flat across the extraction aperture. An IACHEC model of the source was adopted in the fitting<sup>1</sup>. Again, only a global normalisation was allowed to vary. In table 3 we include the fit statistics derived for the source from each observation using the old and new redistribution functions. As

<sup>1</sup>N132D.E0310.v2.11.20180406.mdl

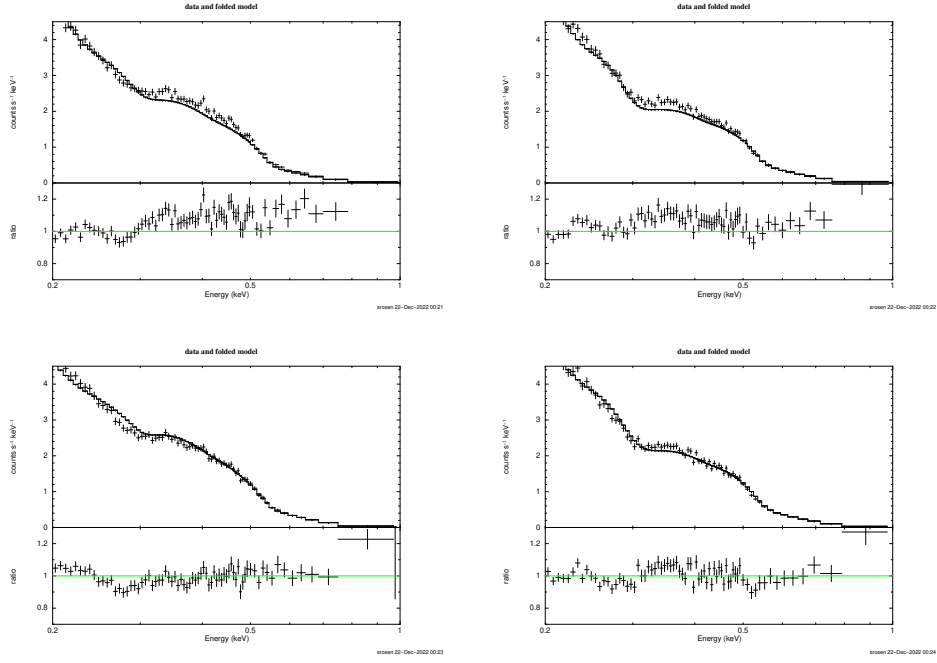


Figure 4: As for figure 3 but for the observation of RX J1856.5-3754 in revolution 3903

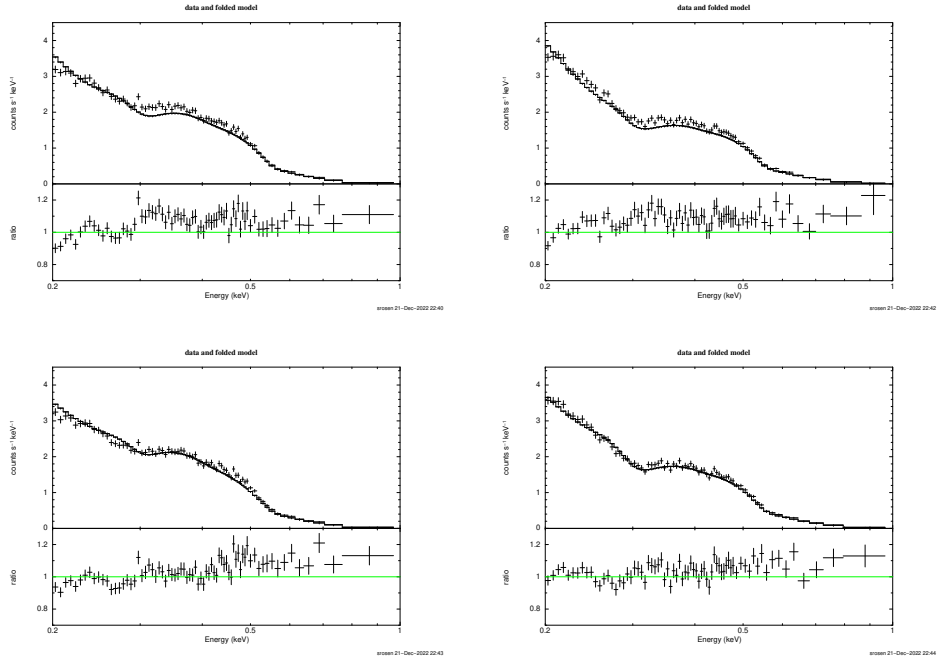


Figure 5: As for figure 3 but for the observation of RX J1856.5-3754 in revolution 4000

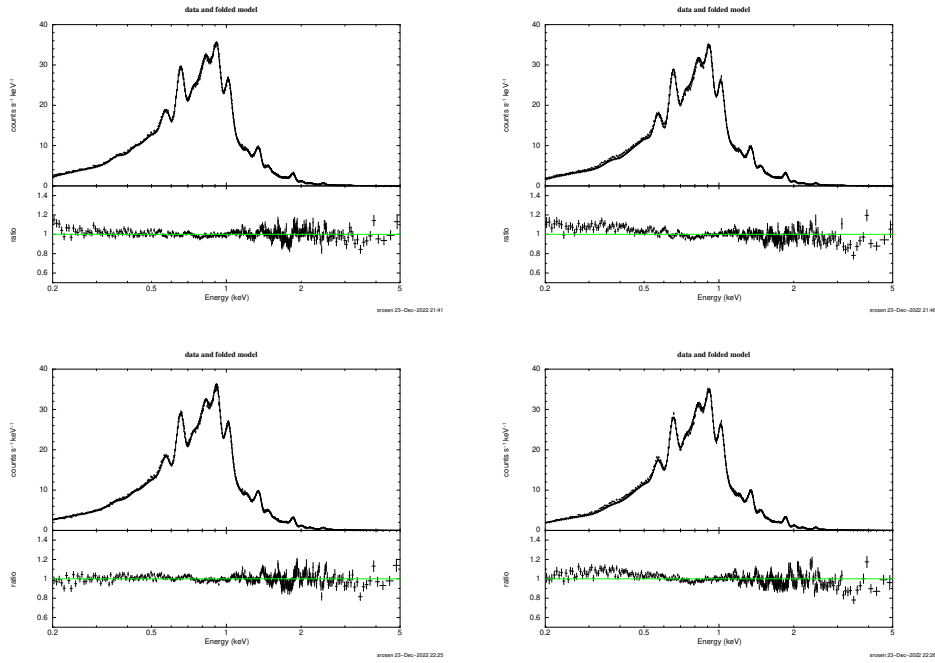


Figure 6: As for figure 3 but for the observation of N132D in revolution 2593

for RX J1856.5-3754, in most cases, the fits using the new response matrix file (RMF) CCFs yield notably lower  $\chi^2$  values than when using the old ones, indicating improved consistency with the models, principally at energies below 1 keV. The improvement in the fits is generally evident in figures 6, 7, 8, 9; the improvement is generally more notable in MOS1 than MOS2, with a more prominent residual excess for  $0.3 < E < 0.5$  keV in MOS2.

An observation of the neutron star, RX J0720.4-3125, from revolution 3636 was also analysed. For this, we took the model of Hohle et al (2012), which involves a blackbody continuum, with an additional Gaussian absorption line. Pn data in the 0.2-1.5 keV range were extracted from an annulus to minimise pile-up. Adopting the same model parameters that Hohle et al reported in revolution 2163, yielded a poor fit. Since Hohle et al. (2012) found the source to show temporal variations, we then fit the pn data from this observation. The best fit blackbody temperature was 85.7 eV but the absorption line energy is at 0.25 keV with equivalent width 72 eV, yielding a  $\chi^2 = 38.2$  for 28 dof. The MOS data were then fit with this model, with the blackbody and Gaussian parameters fixed except for their normalisations. For MOS1 the fit worsens when using the new response CCF (from  $\chi^2=296.2$  to 415.8 for 200 dof). This mainly manifests itself as a deficit of the data at  $0.35 < E < 0.45$  keV - the fits are shown in figure 10. The MOS2 data also yields a slightly worse fit using the new responses (from  $\chi^2=292.8$  to 321.7 for 200 dof). However, the applicability of the model involving the Gaussian absorption component is uncertain, especially given the difference in its centroid, and could result in differences between pn and MOS.

We further investigated the effect of using the new RMF CCFs on a sample of 37 obser-



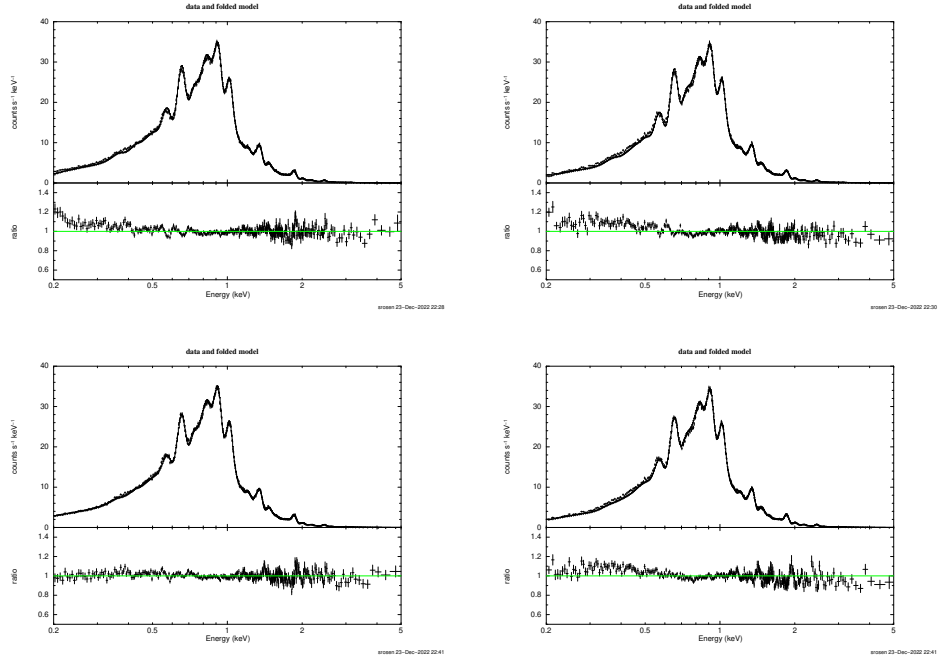


Figure 7: As for figure 3 but for the observation of N132D in revolution 3149

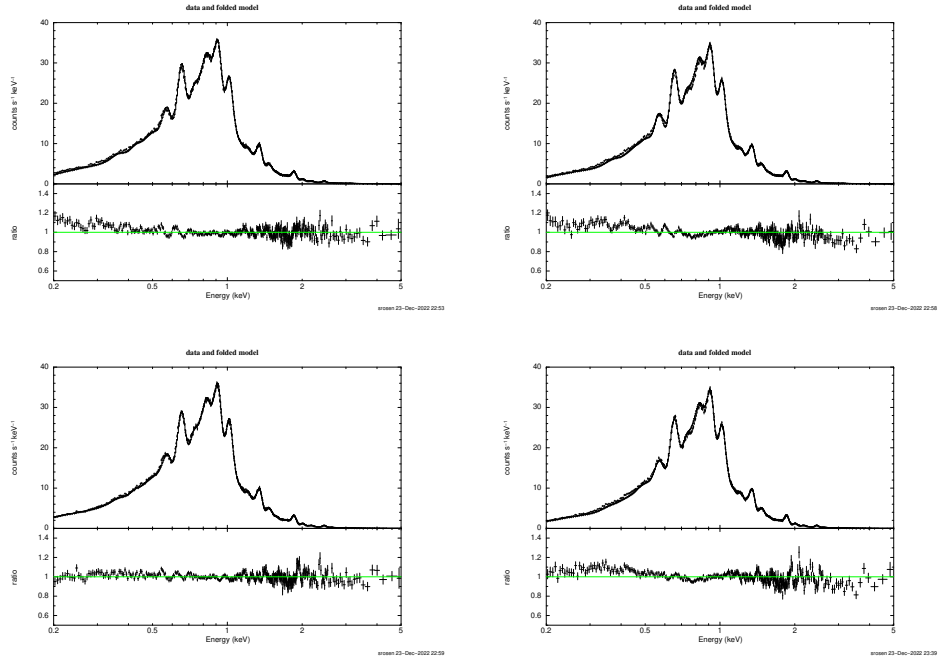


Figure 8: As for figure 3 but for the observation of N132D in revolution 3520

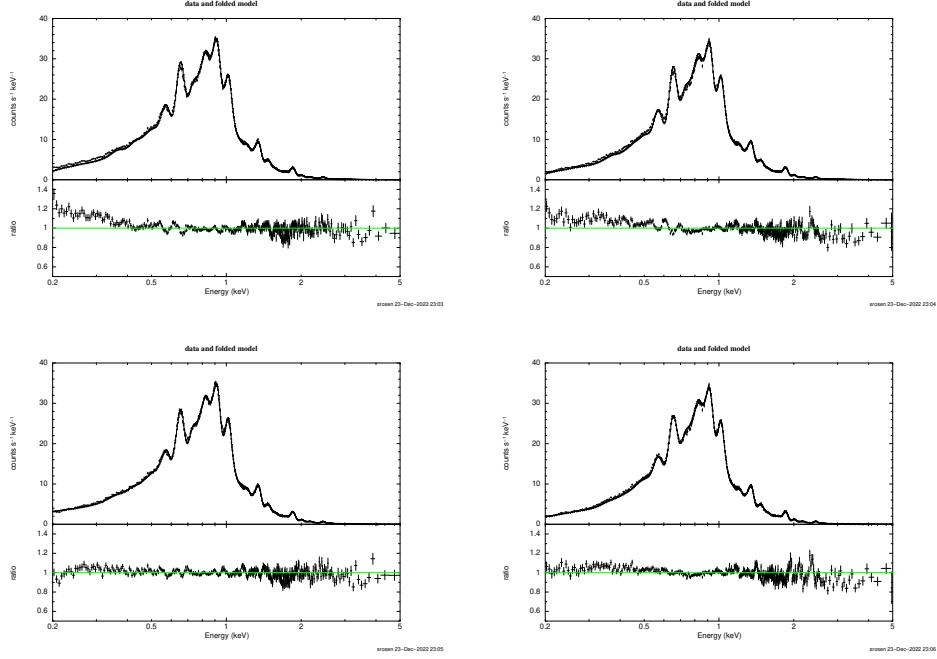


Figure 9: As for figure 3 but for the observation of N132D in revolution 3701

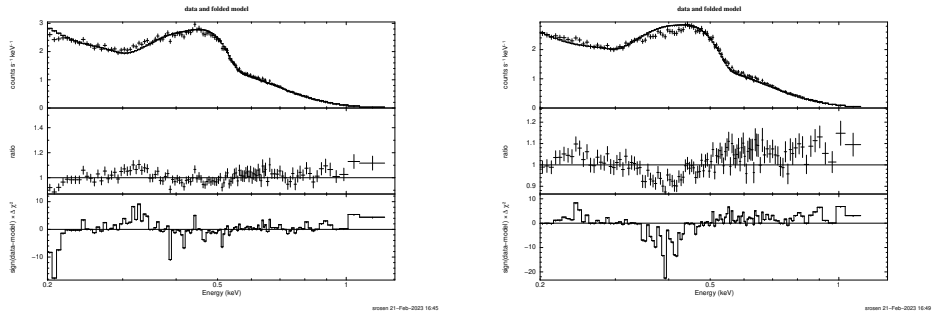


Figure 10: Fits of the pn model (only blackbody and Gaussian normalisations fitted) to the MOS 1 data of RX J0720.4-3125, using the old (left panel) and new (right panel) responses.

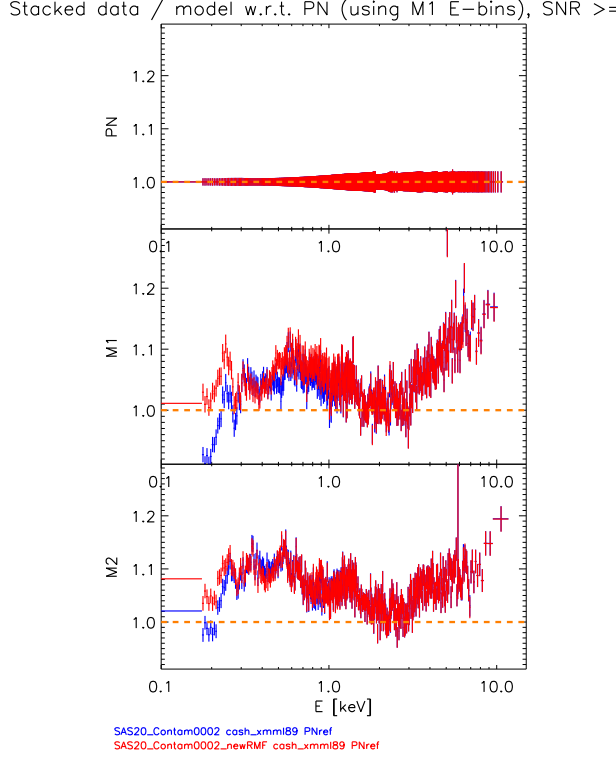


Figure 11: Figure showing a stack of the ratios of the data in each instrument, the ratio for each source being to a model from the literature that is fitted to the PN data and then applied to the MOS data. For the MOS data, the blue curve is based on using the old MOS redistribution CCFs, while the red curve is using the new CCFs.

variations from the effective area analysis performed by Smith et al (XMM-CCF-REL-382). This sample comprises observations of sources, mostly observed on or near the patch, and overlaps with the data from revolutions 2500-3050 (i.e. epochs 15 and 16) discussed here. The results are shown in figure 11. These data suggest there is little change, on average, with respect to the pn, using the new redistribution functions, except, perhaps, for M1 between 0.15 and  $\sim 0.22$  keV. In the  $0.15 < E < 0.3$  keV range, MOS1 and MOS2 data become more consistent. Nevertheless, one must bear in mind that the pn may not be a secure reference and the literature models are not necessarily optimal representations of the data in the low energy range where the effects of redistribution are most prominent. Furthermore, few sources in the sample have strong soft energy output.

### 3.1 Fluxes

To evaluate the impact on fluxes, we computed the MOS1/pn and MOS2/pn flux ratios for the 0.2-0.5 keV band, for 7 on-patch observations of RX J1856.5-3754, based on the 2-component IACHEC model, which are shown in figure 12. For epochs since revolution

2450, we are comparing the fluxes based on the new responses (open squares) against those using the last available update of the response prior to revolution 2450 (filled circles). For the ratios for revolutions 1699 and 1883, which were observed prior to the new epochs included in this update of the responses, only the previous response file is relevant, hence the alignment of the filled circles and open squares for those two revolutions.

Several points emerge. Firstly, this subset of data from RX J1856.5-3754 illustrates that the MOS2 fluxes are systematically higher than MOS1, by around 10-13%; MOS1/pn flux ratios have a mean of 1.10 and 1.05 when using the new and old responses (and current contamination model) respectively, while for MOS2, the corresponding mean ratios are 1.20 and 1.18. This difference between MOS1 and MOS2 was not apparent in the sample of objects used in the effective area analysis reported in XMM-CCF-REL-382 but it should be noted that RX J1856.5-3754 is a much softer source than most objects in that sample. Secondly, use of the new responses increases the fluxes by  $\sim 2$ -5% for the MOS cameras. Thirdly, use of the new contamination model yields MOS1 and MOS2 fluxes up to  $\sim 5\%$  higher, respectively, than when using the old contamination model (see also XMM-CCF-REL-390). Fourthly, the overall trend of the flux ratios is, nevertheless, broadly constant, with scatter of around 4% (MOS1) and 2% (MOS2), indicating that the combination of response and contamination model will result in corrections that maintain relative temporal stability for constant sources.

## 4 Estimated Scientific Quality

Indications from two sources with stable, well defined spectral models suggest the redistribution profiles for the new epochs reduce the deviations of the MOS data from the models at energies below 1 keV, in particular for MOS1 where deviations may be reduced by 5-15% in the  $0.2 < E < 0.5$  keV range. There is little evidence of a significant overall improvement, except at  $E < 0.3$  keV, based on a sample of sources, although their spectra are probably not so accurately characterised as other sources analysed above, which could contribute to the differences in the MOS residuals relative to pn.

## 5 Test procedures and results

Reponse matrices have been generated for sources observed near to the optical-axis, for a range of dates, for both of the MOS cameras. This successfully tests the creation of RMFs with the new algorithm, for sources, whose photons fall predominantly on the patch and in the wings of the patch.

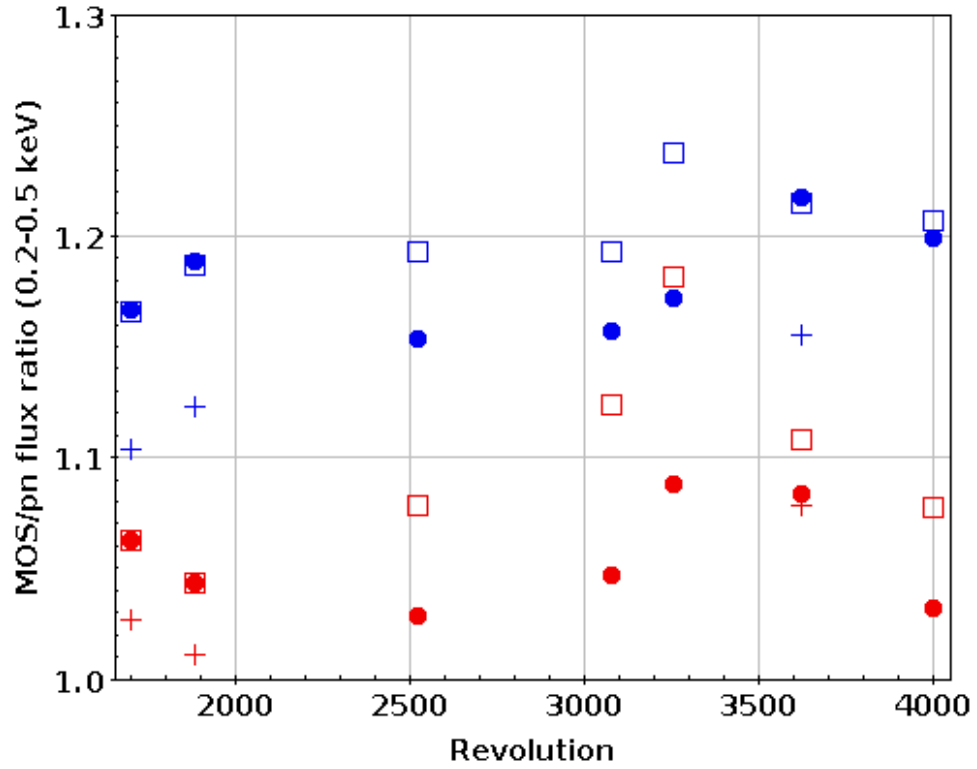


Figure 12: Ratio of MOS1/pn (red) and MOS2/pn (blue) 0.2-0.5 keV band fluxes. Filled circles are using the old response matrices, open squares, the new responses (both using the current contamination model), and crosses (for epochs 1699, 1883 and 3622 only) use the old response and old contamination model.

## 6 Future changes

The MOS redistribution functions will continue to be monitored and updates will be provided for future epochs to take account of their evolution.

### References

Hohle et al., 2012, MNRAS, 423, 1194

Sembay, S, Saxton, R.D., & Guainazzi, M., 2011, XMM-CCF-REL-272 (<https://xmmweb.esac.esa.int/docs/SRN-0272.pdf>)

Rosen, S., et al, 2022, XMM-CCF-REL-390 (<https://xmmweb.esac.esa.int/docs/documents/CAL-SRN-0390-2-2.pdf>)

Table 2: Revolution, observation ID, source observed and position relative to the patch, for the analysis of the new epochs

Revolution	Epoch	Obsid	Source	Location
2521	15	0727760101	RX J1856.5-3754	p
2706	15	0727760301	RX J1856.5-3754	p
2722	15	0412982301	1E 0102-72.3	p
2533	15	0561380601	Zeta Pup	p
2618	15	0727760201	RX J1856.5-3754	o
2722	15	0412982201	1E 0102-72.3	o
2540	15	0159361501	Zeta Pup	o
2909	16	0412982501	1E 0102-72.3	p
2817	16	0561380701	Zeta Pup	p
2989	16	0561380901	Zeta Pup	p
2910	16	0412982401	1E 0102-72.3	o
2794	16	0727760401	RX J1856.5-3754	o
2977	16	0727760601	RX J1856.5-3754	o
2911	16	0561380801	Zeta Pup	o
3111	17	0412983301	1E 0102-72.3	p
3279	17	0412983501	1E 0102-72.3	p
3075	17	0727761001	RX J1856.5-3754	p
3172	17	0561381001	Zeta Pup	p
3092	17	0412983201	1E 0102-72.3	o
3278	17	0412983401	1E 0102-72.3	o
3162	17	0727761101	RX J1856.5-3754	o
3276	17	0561381201	Zeta Pup	o
3459	18	0810880201	1E 0102-72.3	p
3645	18	0810880501	1E 0102-72.3	p
3454	18	0810840101	RX J1856.5-3754	p
3622	18	0810841401	RX J1856.5-3754	p
3361	18	0561381101	Zeta Pup	p
3543	18	0810870101	Zeta Pup	p
3646	18	0810870201	Zeta Pup	p
3459	18	0810880101	1E 0102-72.3	o
3358	18	0727761301	RX J1856.5-3754	o
3542	18	0810840201	RX J1856.5-3754	o
3826	19	0810880701	1E 0102-72.3	p
3804	19	0810841601	RX J1856.5-3754	p
3727	19	0810871301	Zeta Pup	p
3911	19	0810871401	Zeta Pup	p
3652	19	0810880301	1E 0102-72.3	o
3826	19	0810880601	1E 0102-72.3	o
3903	19	0810841701	RX J1856.5-3754	o

Table 3:  $\chi^2$  values in the indicated energy range, for each test source/observation, for MOS1 and MOS2, using the old and the new redistributions functions. Values in parentheses are the degrees of freedom. In the case of N132D, the most luminous parts of the source are positioned outside the patch but the wings extend onto the patch. For RX J1856.5-3754, in the off-patch observation, the object is centred just outside the patch but its wings extend onto the patch.

Rev	Source	Energy range (keV)	M1 (old)	M1 (new)	M2 (old)	M2 (new)	location
3255	RX J1856	0.15-1.0	438.6 (139)	247.5 (140)	512.0 (135)	230.4 (137)	centred within patch
3903	RX J1856	0.15-1.0	622.5 (150)	256.4 (151)	503.9 (148)	269.6 (148)	centred off patch
4000	RX J1856	0.15-1.0	551.0 (141)	301.3 (142)	700.7 (143)	320.0 (143)	centred within patch
2593	N132D	0.15-5.0	1548.5 (801)	1554.3 (801)	2154.3 (792)	1936.9 (795)	centred off patch
3149	N132D	0.15-5.0	1736.0 (754)	1114.3 (754)	1918.8 (754)	1624.9 (748)	centred off patch
3520	N132D	0.15-5.0	2113.8 (786)	1370.1 (788)	2101.7 (783)	1946.9 (779)	centred off patch
3701	N132D	0.15-5.0	3195.1 (792)	1504.9 (791)	2297.8 (787)	1622.9 (789)	centred off patch
2593	N132D	0.20-1.0	377.5 (159)	423.4 (159)	918.6 (159)	757.1 (159)	centred off patch
3149	N132D	0.20-1.0	617.7 (159)	318.4 (159)	956.9 (159)	716.6 (159)	centred off patch
3520	N132D	0.20-1.0	751.1 (159)	401.7 (159)	962.2 (159)	834.1 (159)	centred off patch
3701	N132D	0.20-1.0	1240.3 (159)	474.8 (159)	1177.5 (159)	508.7 (159)	centred off patch